Journal of Materials Chemistry A

ROYAL SOCIETY OF CHEMISTRY

PAPER

View Article Online
View Journal | View Issue

Cite this: *J. Mater. Chem. A*, 2025, **13**, 11382

A highly connected metal–organic framework with stretched inorganic units for propylene/ethylene separation†

Yin Rao,[a] Xinhao Li,[b] Haozhi Xi,[a] Zhongwen Jiang,[a] Wangzhi Li,[a] Han Zhou,[c] Yanping Zhang,[c] Chuixiong Wu,[c] Yue-Biao Zhang[b] and Qiaowei Li*[a]

Received 28th January 2025
Accepted 10th March 2025

DOI: 10.1039/d5ta00771b

rsc.li/materials-a

Separating propylene from ethylene in the product mixture derived from the methanol-to-olefin conversion process in an energy-efficient way is challenging, and adsorptive separation utilizing porous materials such as metal–organic frameworks (MOFs) provides a potential solution. Herein, we constructed a highly connected MOF structure with "stretched" [Zn_8SiO_4] as metal nodes and mixed binding groups (carboxylate and pyrazolate) as linkers. The mixed binding groups adapted well to the increase in the inter-metal distance caused by the insertion of SiO_4^{4-} in the nodes, enabling the formation of a highly symmetrical 12-connected net with high porosity and suitable pore apertures. This framework exhibited an impressive C_3H_6 adsorption capacity of 180.5 $cm^3\ g^{-1}$ and a calculated C_3H_6/C_2H_4 selectivity of 8.6 at 298 K and 100 kPa, which was attributed to the abundant N/O sites on the pore surface that generated stronger interactions with C_3H_6. Furthermore, dynamic breakthrough experiments demonstrated that the framework was capable of effectively separating C_3H_6/C_2H_4 under various conditions, making it a promising benchmark adsorbent for industrial applications.

Introduction

As two of the key olefins in the chemical industry, ethylene (C_2H_4) and propylene (C_3H_6) are crucial raw materials for the production of a wide variety of polymers and organic products. Traditionally, C_2H_4 and C_3H_6 are primarily produced *via* naphtha cracking, a process that relies on fossil resources.[1,2] Recently, sustainable technology for converting methanol to olefins has emerged as an effective alternative for C_2H_4 and C_3H_6 production.[3–5] This process yields products typically consisting of ~51 wt% C_2H_4 and 21 wt% C_3H_6,[6] which need to be separated to efficiently use each component and meet the high-purity requirement for industrial use. Cryogenic distillation is the predominant method for olefin separation; however, cooling the gases to exceedingly low temperatures is markedly energy-intensive.[7] To address this challenge, adsorptive separations utilizing porous materials are being developed as a more energy-efficient technology.[8–10]

MOFs offer significant advantages in terms of tunable pore sizes and functionalities,[11–19] making them particularly suitable for adsorptive separation and purification.[20–26] While MOFs have been widely used to separate various gas mixtures, the separation of C_3H_6 and C_2H_4 is still a great challenge. Their kinetic diameters are very similar (C_3H_6, 4.68 Å; C_2H_4, 4.16 Å),[22] making their size-/shape-selective separation difficult. Therefore, designing differentiated interaction sites in the porous MOFs is a prerequisite for achieving a high separation selectivity.[27,28] On the one hand, higher polarizability of C_3H_6 (62.6×10^{-25} cm^3) suggests stronger dispersion forces with the framework than C_2H_4 (42.5×10^{-25} cm^3).[22] On the other hand, the interaction difference can be further amplified by introducing more weak-to-medium interactions, such as C–H···O/N hydrogen bonds and C–H···π interactions, between the framework and the guests.[29,30]

Herein, we synthesized an MOF structure by the reticulation between a relatively rare [Zn_8SiO_4]-based secondary building unit (SBU) and 4-(1*H*-pyrazol-4-yl)benzoic acid (H_2PyBC). Compared with the traditional Zn–carboxylate MOFs, the SiO_4^{4-} in the SBU centre "stretched" the SBU size, and the mixed binding groups (carboxylate and pyrazolate) prompted its pointing direction to take on a cuboctahedron geometry, which further guided the overall framework into an **fcu** net with 12-connected (12-c) nodes. The framework exhibited a Brunauer–Emmett–Teller (BET) surface area of 1965 $m^2\ g^{-1}$, with the pore

[a]*Department of Chemistry, State Key Laboratory of Porous Materials for Separation and Conversion, Collaborative Innovation Center of Chemistry for Energy Materials, Shanghai Key Laboratory of Molecular Catalysis and Innovative Materials, Fudan University, Shanghai 200433, P. R. China. E-mail: qwli@fudan.edu.cn*

[b]*School of Physical Science and Technology, Shanghai Key Laboratory of High-Resolution Electron Microscopy, State Key Laboratory of Advanced Medical Materials and Devices, ShanghaiTech University, Shanghai 201210, P. R. China*

[c]*Suzhou MiQro Era Quantum Technology Ltd, Jiangsu 215011, P. R. China*

† Electronic supplementary information (ESI) available. CCDC 2418870 and 2418871. For ESI and crystallographic data in CIF or other electronic format see DOI: https://doi.org/10.1039/d5ta00771b

size concentrated at 7.9 and 13.0 Å. Interestingly, the C_3H_6 adsorption capacity of the MOF reached 180.5 $cm^3\ g^{-1}$ at 298 K and 100 kPa, while the C_2H_4 uptake was merely 68.2 $cm^3\ g^{-1}$, indicating a stronger interaction between C_3H_6 and the framework. Grand canonical Monte Carlo (GCMC) simulations revealed a binding energy difference of 10.11 kJ mol^{-1} for C_3H_6 and C_2H_4 when they interacted with the strongest binding sites on the backbone. Furthermore, dynamic breakthrough experiments concluded that for an equimolar C_3H_6/C_2H_4 mixture, the breakthrough time interval reaches 41.3 min at 298 K and maintains 35.3 min at 328 K, suggesting the potential of applying this MOF for C_3H_6/C_2H_4 separation.

Experimental

Synthesis of FDM-201

A screening of the reaction conditions was carried out by using H_2PyBC and $Zn(NO_3)_2\cdot 6H_2O$ as the main reactants with various modulators in 2.0 mL solvents. After the FDM-201 single crystals were obtained, the preparation was further scaled up proportionally.

Specifically, $Zn(NO_3)_2\cdot 6H_2O$ (2340 mg, 7.87 mmol), H_2PyBC (168 mg, 0.89 mmol), and 1*H*-benzotriazole (HBTA, 220 mg, 1.85 mmol) are dissolved in 34.0 mL *N*,*N*-dimethylformamide (DMF) in a 100 mL pressure-resistant tube with a Teflon cap. 6.0 mL aqueous Na_2SiO_3 solution (0.015 M) is further added. After sonication, the tube with the clear solution is placed in an oven at 115 °C for 12 h, and colorless octahedral crystals are obtained. Yield: 73.0 mg, *i.e.*, 47% based on Na_2SiO_3.

Results and discussion

Colourless octahedral crystals of FDM-201 are synthesized *via* a solvothermal reaction using $Zn(NO_3)_2\cdot 6H_2O$, H_2PyBC, and $Na_2SiO_3\cdot 9H_2O$ in a mixed solvent of DMF and water at 115 °C for 12 h. HBTA is introduced into the solution as a structural modulator to slow down the reaction and obtain high-quality single crystals of FDM-201. Single-crystal X-ray diffraction (SXRD) reveals that FDM-201 crystallizes in the cubic space group $Fm\bar{3}m$, with $a = 23.76$ Å. In the structure, each O in the SiO_4^{4-} bridges two Zn(II) to form a node with a cubic $[Zn_8SiO_4]$ core (Fig. 1a). Each Zn(II) in the node is further coordinated with three N/O from the PyBC linkers (Fig. 1b and c), and twelve PyBC linkers are bound to the $[Zn_8SiO_4]$ core. As a result, a three-dimensional (3D) network with the **fcu** topology (Fig. 1d) is reticulated by the 12-c cuboctahedral nodes and the PyBC linkers. It should be noted that the orientational disorder of PyBC is observed (Fig. S1†) due to the approximate interatomic distances between the coordinating atoms (O or N) within both the carboxylate and pyrazolate groups.

Although two MOFs with the same $[Zn_8SiO_4]$ nodes have been previously reported,[31,32] each node in the FDM-201 is connected to twelve neighbouring nodes, while formerly it tended to connect with only 6 or 8 nodes through the linker pairs (Fig. 2),[31] and the binding groups were pure carboxylate rather than mixed carboxylate/pyrazolate. Compared with the conventional $Zn_4O(COO)_6$ (ref. 18) and $Zn(NN)_2$ (ref. 33 and 34) SBUs (Fig. 2a), the inter-metal distances in the $[Zn_8SiO_4]$ nodes are lengthened because of the insertion of SiO_4^{4-} in the SBU centre, making the SBU "stretched". Moreover, in order to cope with this SBU stretch, the metal–linker coordination needs to be distorted. Compared to the metal–pyrazolate linkage in FDM-201, the metal–carboxylate linkage in the previous example[31] shows a higher degree of flexibility (Fig. 2b and c), causing the O–Zn···SiO···Zn–O moiety to deviate from a planar configuration when the Zn···Zn distance is lengthened. As a result, the "pairing" of neighbouring ligands in parallel directions in the pure carboxylate version is evident, making the SBU six-connected. With less distortion in the N–Zn···SiO···Zn–N, the configuration of the SBU with mixed carboxylate/pyrazolate adopts a cuboctahedral geometry in FDM-201. Overall, the binding group difference (carboxylate *vs.* pyrazolate) imposes different distortion extents in the metal coordination sphere and consequently influences the connecting directions of the stretched SBUs.

The powder X-ray diffraction (PXRD) pattern of the as-synthesized FDM-201 matches with the corresponding simulated pattern, confirming its crystallinity and phase purity

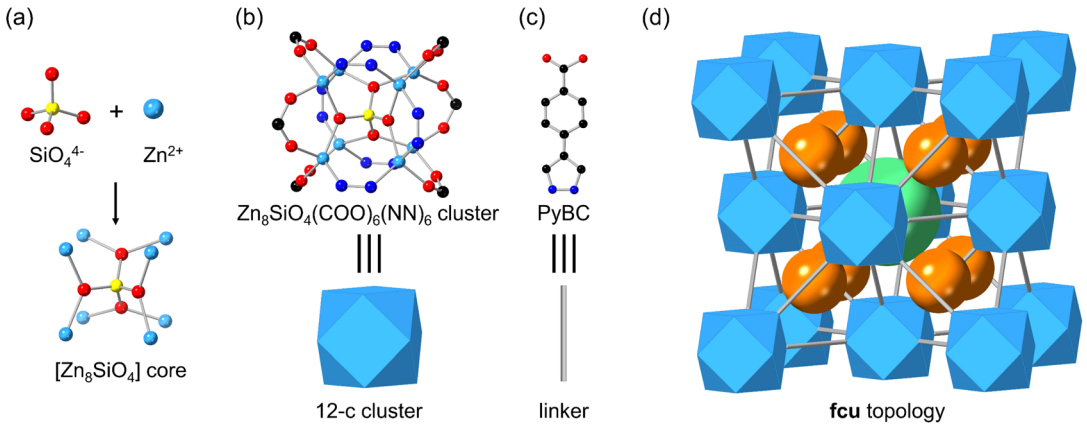

Fig. 1 Crystal structure of FDM-201. (a) A $[Zn_8SiO_4]$ core is constructed by eight Zn(II) and a SiO_4^{4-}. (b) The 12-connected units based on the $[Zn_8SiO_4]$ cores are connected with (c) the PyBC linkers to afford (d) an MOF structure with the **fcu** topology. The octahedral cage and the tetrahedral cages are displayed as green and orange spheres. Atom colour code: Zn, light blue; Si, yellow; O, red; N, dark blue; C, black.

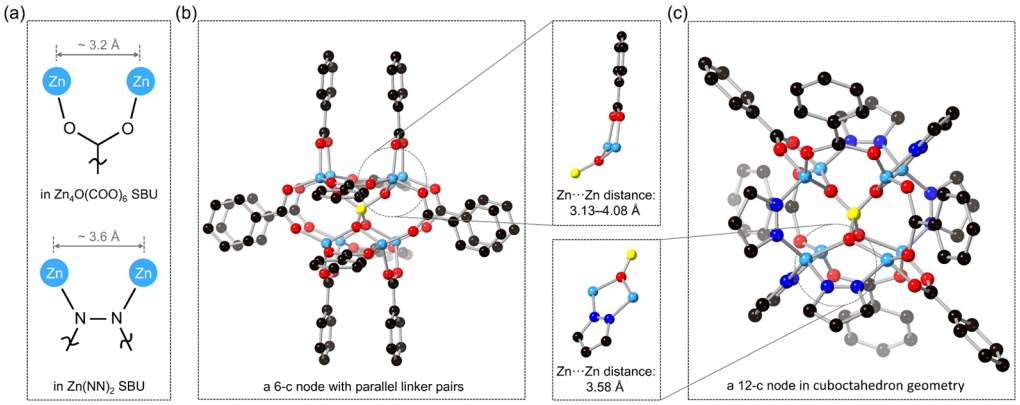

Fig. 2 Control of distinct coordination linkages giving rise to $[Zn_8(SiO_4)(C_8H_4O_4)_6]_n$[31] and FDM-201 with different topologies. (a) Typical Zn···Zn distance in the conventional $Zn_4O(COO)_6$ and $Zn(NN)_2$ units. (b) SBU in $[Zn_8(SiO_4)(C_8H_4O_4)_6]_n$ can be viewed as 6-c because the twelve linkers are organized into six pairs owing to the distortion in the O–Zn···SiO···Zn–O moiety. (c) SBU in FDM-201 showing cuboctahedron geometry, in which the O–Zn···SiO···Zn–O moiety is coplanar.

(Fig. 3a). The as-synthesized sample can be successfully activated by solvent exchange with acetone, followed by heating at 80 °C under vacuum. The sharp peaks in the PXRD pattern match well with those from the corresponding as-synthesized sample, indicating that it maintains high crystallinity after activation (Fig. 3a). Furthermore, FDM-201 possesses outstanding thermal stability, with no significant weight loss observed in the thermogravimetric analysis (TGA) until it reaches 450 °C in an air atmosphere (Fig. S6†). The crystals retain sharp PXRD peaks after being immersed in water for 6 h (Fig. S7†), although soaking for a longer time would induce a structural transformation. A diffraction peak ($2\theta = 6.9°$) corresponding to a new condensed structure with a formula of $Zn_2PyBC(OH)_2$ (Fig. S2, S8, and S9, see the discussion in the ESI†) emerges in the PXRD after being immersed in H_2O for 12 h, and the peak becomes more evident after 1 day (Fig. S8†). Immersing the crystals in boiling water would accelerate the structural transformation, as indicated by the completely new phase after 1 day (Fig. S8†). However, after soaking the FDM-201 crystals in a mixed H_2O/DMF solvent (v/v, 4 : 1) for 7 days, we found that the structure is retained (Fig. S7†).

The crystal structure of FDM-201 reveals that it features two types of cages: an octahedral cage with an inscribed sphere diameter of 13.4 Å and a tetrahedral cage with 5.4 Å in diameter, with the assumption that the linkers do not rotate. Based on Zeo++ calculation,[35] the simulated surface area of FDM-201 is 1898 $m^2 g^{-1}$, and its simulated pore volume is 0.70 $cm^3 g^{-1}$. Five parallel 87 K Ar adsorption isotherms are measured to experimentally verify the consistent and permanent porosity of FDM-201 (see Fig. 3b for one isotherm and Fig. S10† for all isotherms). The isotherms exhibit typical type I adsorptions, with a maximum Ar adsorption capacity of 583 ± 6 $cm^3 g^{-1}$ at $P/P_0 = 0.99$. The BET surface area and pore volume of FDM-201 are calculated to be 1965 ± 37 $m^2 g^{-1}$ and 0.74 ± 0.01 $cm^3 g^{-1}$, respectively. The pore size distribution of FDM-201 is further analysed using the isotherm in Fig. 3b and a kernel based on the nonlocal density functional theory (NLDFT). The analysis reveals that the pore size distribution spans two intervals, from 6.1 to 10.5 Å and from 10.5 to 16.2 Å, with predominant concentrations at 7.9 and 13.0 Å, respectively (Fig. 3c). These values align approximately with theoretical predictions, indicating that the pores within the periodic and robust framework remain highly accessible after the activation.

The high BET surface area and pore volume of FDM-201, coupled with the abundant O/N interaction sites on the pore surfaces, intrigued us to explore its potential application in gas adsorption and separation. For gas separation, not only the pore size but also their apertures are critical. Analysis of the FDM-201

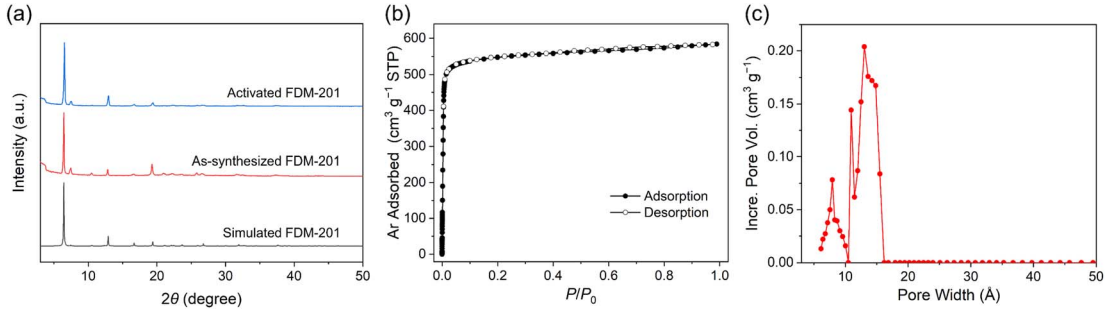

Fig. 3 Physical characterizations of FDM-201. (a) PXRD patterns of the simulated, as-synthesized, and activated FDM-201. (b) 87 K Ar adsorption isotherm of FDM-201. (c) Pore size distribution profile of FDM-201.

crystal structure further reveals that the octahedral and tetrahedral cages have relatively small apertures (triangles with an incircle of 3.9 Å) and make the pores inaccessible to C_3H_6 (kinetic diameter, 4.68 Å) and C_2H_4 (kinetic diameter, 4.16 Å). However, it should be noted that the benzene ring in the PyBC linker can easily rotate at ambient temperature,[36] leading to a "widening" of the pore aperture and an increase in the pore size. After considering the linker rotation, the sizes of the octahedral cage, tetrahedral cage, and pore aperture become 13.4, 8.3, and 6.2 Å. As a result, C_3H_6 and C_2H_4 can indeed be adsorbed by the FDM-201 framework.

To investigate the C_3H_6 and C_2H_4 adsorption capability of FDM-201 in experiments, single-component adsorption isotherms at 273, 298, and 328 K are collected (Fig. 4a and b). FDM-201 exhibits an adsorption uptake of 180.5 $cm^3\ g^{-1}$ for C_3H_6 at 298 K and 1 bar, much higher than that of the C_2H_4 case (68.2 $cm^3\ g^{-1}$). In addition, the adsorption capacity of C_3H_6/C_2H_4 is 200.5/108.4 $cm^3\ g^{-1}$ at 273 K and 137.4/31.6 $cm^3\ g^{-1}$ at 328 K. Remarkably, its C_3H_6 adsorption capacity at 298 K (180.5 $cm^3\ g^{-1}$) is among the many high-performance MOFs, such as spe-MOF (236.9 $cm^3\ g^{-1}$),[37] FJI-H8-Me (211.0 $cm^3\ g^{-1}$),[28] NEM-4 (197.4 $cm^3\ g^{-1}$),[38] MAC-4 (127.0 $cm^3\ g^{-1}$),[39] and CoV-bco-tpt (110.0 $cm^3\ g^{-1}$)[40] (see Table S7 in the ESI† for a summary of the C_3H_6 adsorption capacity of benchmark MOFs). The higher uptake of C_3H_6 than that of C_2H_4 under the tested temperature range suggests that FDM-201 is a potential candidate for C_3H_6/C_2H_4 separation.

Isosteric heat of adsorption (Q_{st}) is calculated based on the single-component gas adsorption isotherms at 273 and 298 K, employing the Clausius–Clapeyron equation (Table S4 and Fig. S11 and S12, see the ESI†). At zero coverage, the Q_{st} values of FDM-201 for C_3H_6 and C_2H_4 are 27.1 and 19.1 kJ mol^{-1}, respectively (Fig. 4c). The notably higher Q_{st} for C_3H_6 confirms stronger interaction between C_3H_6 and the framework, and it is preferably adsorbed (see Table S5† for a summary of Q_{st} values of benchmark MOFs). It is worth noting that the Q_{st} value for C_3H_6 at high coverage is apparently higher than the value at zero coverage, indicating that at a high-pressure range, the C_3H_6–C_3H_6 interaction is stronger than the C_3H_6–framework interaction.

To preliminarily evaluate the C_3H_6/C_2H_4 separation performance of FDM-201, the ideal adsorption solution theory (IAST) is employed to calculate the selectivity (Table S6 and Fig. S13†). For an equimolar C_3H_6/C_2H_4 mixture at 100 kPa, the calculated selectivities at 273, 298, and 328 K are 11.9, 8.6, and 7.7, respectively (Fig. 4d). The selectivity at 298 K is comparable with that of the current outstanding materials, such as HOF-NBDA (11.1),[41] MAC-4 (9.5),[39] and JLU-MOF132 (9.2),[42] (Table S7†). Combined with the high adsorption capacity (C_3H_6, 180.5 $cm^3\ g^{-1}$), FDM-201 appears to be a fairly good option among the known materials for C_3H_6/C_2H_4 separation (Fig. 4e and Table S7†). Impressively, the selectivity only drops slightly to 7.7 at 328 K, suggesting a high selectivity even at a relatively elevated temperature proximate to the actual operating condition.[43] The IAST selectivity of FDM-201 for the C_3H_6/C_2H_4 mixtures at 20/50 and 10/90 (v/v) ratios are further calculated,[37,44] and the framework maintains a high selectivity of 14.1/9.4/7.3 for C_3H_6/C_2H_4 (v/v, 20/50) at 273/298/328 K, and 14.8/9.4/7.2 for C_3H_6/C_2H_4 (v/v, 10/90) at these three temperatures (Fig. S14 and Table S8†).

Separation potential (Δq) is a comprehensive metric that combines both adsorption capacity and selectivity to evaluate the separation ability of materials.[45] For C_3H_6-selective

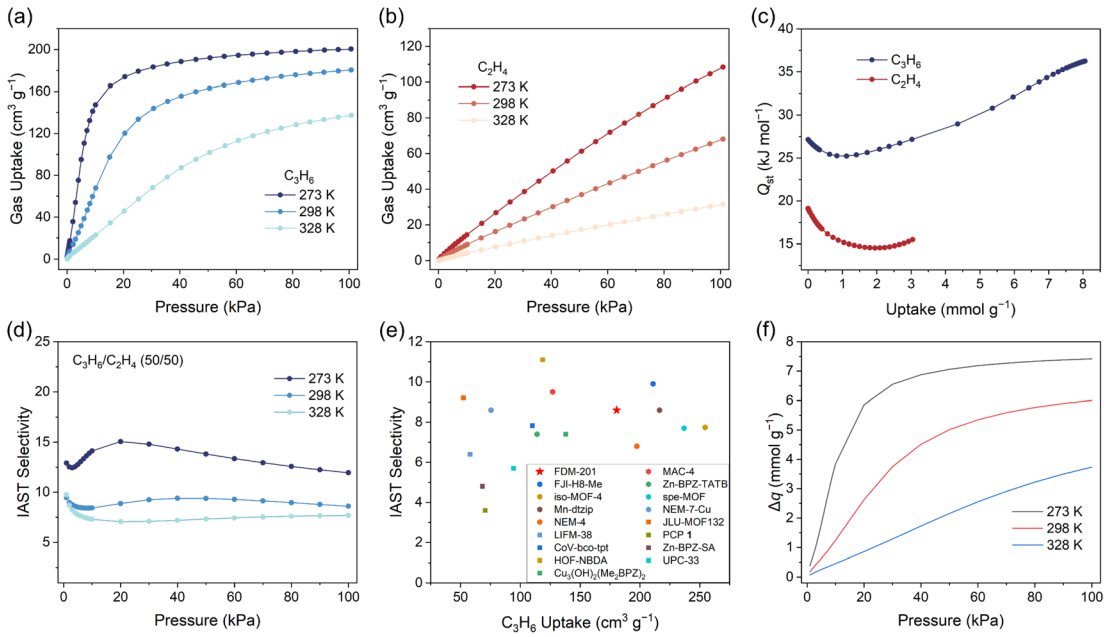

Fig. 4 Adsorption studies of FDM-201. (a) C_3H_6 and (b) C_2H_4 adsorption isotherms at 273, 298, and 328 K, respectively. (c) Q_{st} curves for C_3H_6 and C_2H_4. (d) IAST selectivity for equimolar C_3H_6/C_2H_4 at 273, 298, and 328 K. (e) Comparison of the C_3H_6 uptake and IAST selectivity between FDM-201 and the representative C_3H_6-selective MOF adsorbents. (f) Separation potential of FDM-201 for the equimolar C_3H_6/C_2H_4 mixture at 273, 298, and 328 K.

adsorbents, Δq presents a reliable prediction of the maximum amount of pure C_2H_4 recovered during a fixed-bed separation process. According to the IAST results on equimolar mixtures, Δq is calculated to be 7.42, 6.00, and 3.73 mmol g^{-1} at 273, 298, and 328 K, respectively (Fig. 4f). The Δq value for FDM-201 at 298 K is much higher than some benchmark C_3H_6/C_2H_4 separating-MOFs, such as MAC-4 (4.4 mmol g^{-1}),[39] Zn-BPZ-TATB (3.74 mmol g^{-1}),[30] Zn-BPZ-SA (1.92 mmol g^{-1}),[46] and $Zn_2(oba)_2(dmimpym)$ (3.04 mmol g^{-1}).[47]

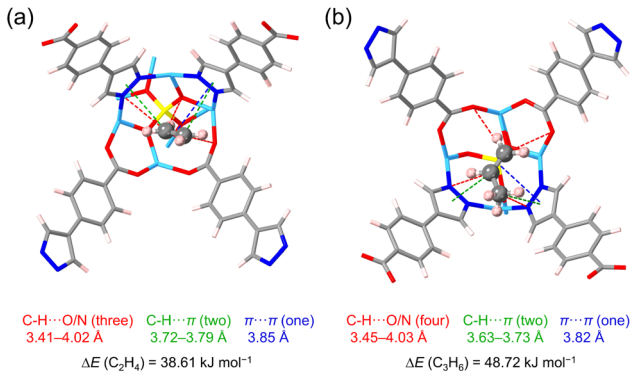

Fig. 5 Interactions between the preferential binding site and (a) C_2H_4 and (b) C_3H_6. Atom colour code: Zn, light blue; Si, yellow; O, red; N, dark blue; C, grey; H, pink.

To gain a deep understanding of the interactions between the framework and the adsorbates, GCMC simulations are employed to investigate the preferential binding sites within the octahedral cage of FDM-201 for C_2H_4 and C_3H_6. For both gases, the strongest adsorption sites, with multiple supramolecular interactions between the backbone and the guests, are located near the $[Zn_8SiO_4]$ core (Fig. 5). Specifically, three C–H···O/N hydrogen bonds (C···O/N bond length: 3.41–4.02 Å), two C–H···π interactions (3.72–3.79 Å) and one π···π interaction (3.85 Å) exist between one C_2H_4 and this site in FDM-201. The calculated binding energy is 38.61 kJ mol^{-1}. On the other hand, stronger interaction with four C–H···O/N hydrogen bonds (3.45–4.03 Å), two C–H···π interactions (3.63–3.73 Å), and one π···π interaction (3.82 Å) enabled the binding energy of C_3H_6 to this site to be 48.72 kJ mol^{-1}. Based on the simulation, the difference in the static binding energies between C_3H_6 and C_2H_4 is 10.11 kJ mol^{-1}, which is roughly in agreement with the difference in the Q_{st} calculated from the adsorption isotherms (8.0 kJ mol^{-1}) and corroborates with the preferred C_3H_6 adsorption in FDM-201.

To verify the actual C_3H_6/C_2H_4 separation performance, dynamic breakthrough experiments for binary C_3H_6/C_2H_4 (v/v, 50/50) mixtures are conducted at 298 and 328 K. Before the experiments, the acetone-exchanged sample is activated under vacuum at 80 °C for 12 h. Subsequently, it is packed into a stainless-steel column (l = 15 cm, d = 0.42 cm). The packed column is firstly purged with He at a flow rate of 20 mL min^{-1}

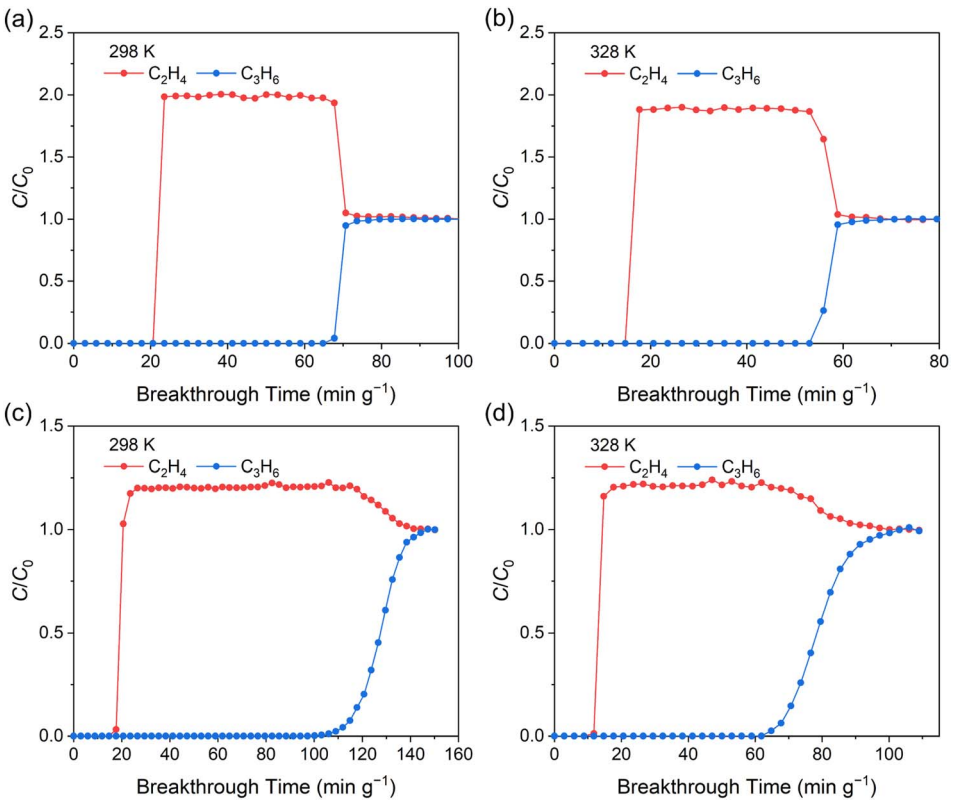

Fig. 6 Breakthrough curves for C_3H_6/C_2H_4-based mixtures under a flow of 5 mL min^{-1} for FDM-201 in a packed column. The testing conditions are (a) C_3H_6/C_2H_4 (v/v, 50/50) at 298 K, (b) C_3H_6/C_2H_4 (v/v, 50/50) at 328 K, (c) C_3H_6/C_2H_4/He (v/v/v, 20/50/30) at 298 K, and (d) C_3H_6/C_2H_4/He (v/v/v, 20/50/30) at 328 K.

for 30 min. At 298 K, under a mixed gas flow (flow rate, 5 mL min^{-1}), C_2H_4 first elutes from the column at 23.5 min, whereas C_3H_6 is under detection limit until 64.8 min (Fig. 6a). The breakthrough time interval, during which high-grade C_2H_4 can be collected, is calculated to be 41.3 min. At 328 K, FDM-201 can still efficiently separate C_3H_6 and C_2H_4, with an interval of 35.3 min (Fig. 6b). Furthermore, when the feed gas composition is adjusted to 20 : 50 : 30 (v/v/v, C_3H_6 to C_2H_4 to He, with the C_3H_6/C_2H_4 ratio close to the application scenario), FDM-201 continues to exhibit effective separation performance with the interval time being 82.4 and 53.0 min at 298 and 328 K, respectively (Fig. 6c and d). The breakthrough experiments have proved that FDM-201 is a promising candidate for highly efficient propylene/ethylene separation across different composition ratios and different temperatures.

Conclusion

In summary, we report the synthesis of a highly connected MOF structure with $[Zn_8SiO_4]$-based metal nodes. The embedding of the SiO_4^{4-} anion into the Zn_8 cube stretches the distance between the Zn(II) atoms, rendering the mixed pyrazolate/carboxylate binding groups an appropriate choice to maintain the inorganic unit in a highly symmetrical cuboctahedral geometry. The obtained FDM-201 with **fcu** topology exhibits a high BET surface area of 1965 $m^2 g^{-1}$, with pore sizes enabling high-capacity accessibility for both propylene and ethylene gas molecules. Moreover, the abundant N/O sites in FDM-201 provide a stronger affinity with propylene, making it a potential candidate for propylene/ethylene separation. This is evidenced by the single-component adsorption isotherms, IAST selectivity calculation, and adsorptive interaction simulations. Dynamic breakthrough experiments demonstrate that FDM-201 is capable of effectively separating equimolar C_3H_6/C_2H_4, with the breakthrough time interval reaching 41.3 min at 298 K. Overall, this study proposes that the selection of binding groups can modify the connectivity of a stretched SBU, thereby enabling the creation of subsequent MOFs with appropriate sizes and functionalities for gas separation applications.

Data availability

The data supporting this article have been included as part of the ESI.† Crystallographic data for FDM-201 and $Zn_2PyBC(OH)_2$ have been deposited at the Cambridge Crystallographic Data Centre with the CCDC numbers 2418870 and 2418871 and can be obtained from **https://www.ccdc.cam.ac.uk/**.

Author contributions

Y. Rao: investigation, formal analysis, visualization, validation, writing – original draft. X. Li: formal analysis. H. Xi: formal analysis. Z. Jiang: formal analysis. W. Li: formal analysis. H. Zhou: formal analysis. Y. Zhang: formal analysis. C. Wu: formal analysis. Y.-B. Zhang: supervision. Q. Li: conceptualization, investigation, funding acquisition, supervision, writing – review & editing.

Conflicts of interest

There are no conflicts to declare.

Acknowledgements

This work was supported by the National Key Research and Development Project of China (Grant 2018YFA0209401), the National Natural Science Foundation of China (Grants 21922103, 21961132003, and 22088101), and the Science and Technology Commission of Shanghai Municipality (Grant 2024ZDSYS02).

References

1 S. M. Sadrameli, *Fuel*, 2015, **140**, 102–115.
2 A. Corma, E. Corresa, Y. Mathieu, L. Sauvanaud, S. Al-Bogami, M. S. Al-Ghrami and A. Bourane, *Catal. Sci. Technol.*, 2017, **7**, 12–46.
3 M. R. Gogate, *Pet. Sci. Technol.*, 2019, **37**, 559–565.
4 P. Tian, Y. Wei, M. Ye and Z. Liu, *ACS Catal.*, 2015, **5**, 1922–1938.
5 U. Olsbye, S. Svelle, M. Bjørgen, P. Beato, T. V. W. Janssens, F. Joensen, S. Bordiga and K. P. Lillerud, *Angew. Chem., Int. Ed.*, 2012, **51**, 5810–5831.
6 C. Wang, L. Yang, M. Gao, X. Shao, W. Dai, G. Wu, N. Guan, Z. Xu, M. Ye and L. Li, *J. Am. Chem. Soc.*, 2022, **144**, 21408–21416.
7 D. S. Sholl and R. P. Lively, *Nature*, 2016, **532**, 435–437.
8 Y. Wu and B. M. Weckhuysen, *Angew. Chem., Int. Ed.*, 2021, **60**, 18930–18949.
9 P. J. Bereciartua, A. Cantin, A. Corma, J. L. Jorda, M. Palomino, F. Rey, S. Valencia, E. W. Corcoran Jr., P. Kortunov, P. I. Ravikovitch, A. Burton, C. Yoon, Y. Wang, C. Paur, J. Guzman, A. R. Bishop and G. L. Casty, *Science*, 2017, **358**, 1068–1071.
10 Y. Wang, S. B. Peh and D. Zhao, *Small*, 2019, **15**, 1900058.
11 S. Kitagawa, R. Kitaura and S.-i. Noro, *Angew. Chem., Int. Ed.*, 2004, **43**, 2334–2375.
12 G. Ferey, *Chem. Soc. Rev.*, 2008, **37**, 191–214.
13 J.-P. Zhang, Y.-B. Zhang, J.-B. Lin and X.-M. Chen, *Chem. Rev.*, 2012, **112**, 1001–1033.
14 H. Furukawa, K. E. Cordova, M. O'Keeffe and O. M. Yaghi, *Science*, 2013, **341**, 1230444.
15 B. Li, H.-M. Wen, Y. Cui, W. Zhou, G. Qian and B. Chen, *Adv. Mater.*, 2016, **28**, 8819–8860.
16 S. Yuan, L. Feng, K. Wang, J. Pang, M. Bosch, C. Lollar, Y. Sun, J. Qin, X. Yang, P. Zhang, Q. Wang, L. Zou, Y. Zhang, L. Zhang, Y. Fang, J. Li and H.-C. Zhou, *Adv. Mater.*, 2018, **30**, 1704303.
17 H. Jiang, D. Alezi and M. Eddaoudi, *Nat. Rev. Mater.*, 2021, **6**, 466–487.
18 H. Li, M. Eddaoudi, M. O'Keeffe and O. M. Yaghi, *Nature*, 1999, **402**, 276–279.
19 O. M. Yaghi, G. Li and H. Li, *Nature*, 1995, **378**, 703–706.
20 W. Fan, X. Zhang, Z. Kang, X. Liu and D. Sun, *Coord. Chem. Rev.*, 2021, **443**, 213968.

21 K.-J. Chen, D. G. Madden, S. Mukherjee, T. Pham, K. A. Forrest, A. Kumar, B. Space, J. Kong, Q.-Y. Zhang and M. J. Zaworotko, *Science*, 2019, **366**, 241–246.
22 L. Yang, S. Qian, X. Wang, X. Cui, B. Chen and H. Xing, *Chem. Soc. Rev.*, 2020, **49**, 5359–5406.
23 Y.-J. Tian, C. Deng, L. Zhao, J.-S. Zou, X.-C. Wu, Y. Jia, Z.-Y. Zhang, J. Zhang, Y.-L. Peng, G. Chen and M. J. Zaworotko, *Nat. Chem.*, 2025, **17**, 141–147.
24 D. Wu, P.-F. Zhang, G.-P. Yang, L. Hou, W.-Y. Zhang, Y.-F. Han, P. Liu and Y.-Y. Wang, *Coord. Chem. Rev.*, 2021, **434**, 213709.
25 R.-B. Lin, Z. Zhang and B. Chen, *Acc. Chem. Res.*, 2021, **54**, 3362–3376.
26 X. Zhao, Y. Wang, D.-S. Li, X. Bu and P. Feng, *Adv. Mater.*, 2018, **30**, 1705189.
27 L. Zhang, L.-N. Ma, G.-D. Wang, L. Hou, Z. Zhu and Y.-Y. Wang, *J. Mater. Chem. A*, 2023, **11**, 2343–2348.
28 Z. Di, Z. Ji, C. Chen, R. Krishna, D. Yuan, M. Hong and M. Wu, *Chem. Eng. J.*, 2024, **493**, 152442.
29 G. Zhen, Y. Liu, Y. Zhou, Z. Ji, H. Li, S. Zou, W. Zhang, Y. Li, Y. Liu, C. Chen and M. Wu, *ACS Appl. Mater. Interfaces*, 2024, **16**, 1179–1186.
30 G.-D. Wang, Y.-Z. Li, W. J. Shi, L. Hou, Y.-Y. Wang and Z. Zhu, *Angew. Chem., Int. Ed.*, 2023, **62**, e202311654.
31 S.-Y. Yang, L.-S. Long, Y.-B. Jiang, R.-B. Huang and L.-S. Zheng, *Chem. Mater.*, 2002, **14**, 3229–3231.
32 S.-Y. Yang, L.-S. Long, R.-B. Huang and L.-S. Zheng, *Chem. Commun.*, 2002, 472–473.
33 Y.-S. Wei, L. Sun, M. Wang, J. Hong, L. Zou, H. Liu, Y. Wang, M. Zhang, Z. Liu, Y. Li, S. Horike, K. Suenaga and Q. Xu, *Angew. Chem., Int. Ed.*, 2020, **59**, 16013–16022.
34 C. Pettinari, A. Tabacaru, I. Boldog, K. V. Domasevitch, S. Galli and N. Masciocchi, *Inorg. Chem.*, 2012, **51**, 5235–5245.
35 T. F. Willems, C. Rycroft, M. Kazi, J. C. Meza and M. Haranczyk, *Microporous Mesoporous Mater.*, 2012, **149**, 134–141.
36 A. Gonzalez-Nelson, F.-X. Coudert and M. A. van der Veen, *Nanomaterials*, 2019, **9**, 330.
37 H. Fang, B. Zheng, Z.-H. Zhang, H.-X. Li, D.-X. Xue and J. Bai, *Angew. Chem., Int. Ed.*, 2021, **60**, 16521–16528.
38 X. Liu, W. Fan, M. Zhang, G. Li, H. Liu, D. Sun, L. Zhao, H. Zhu and W. Guo, *Mater. Chem. Front.*, 2018, **2**, 1146–1154.
39 G.-D. Wang, Y.-Z. Li, R. Krishna, W.-Y. Zhang, L. Hou, Y.-Y. Wang and Z. Zhu, *Angew. Chem., Int. Ed.*, 2024, **63**, e202319978.
40 Y. Xiao, A. N. Hong, Y. Chen, H. Yang, Y. Wang, X. Bu and P. Feng, *Small*, 2023, **19**, 2205119.
41 Y. Zhou, C. Chen, Z. Ji, R. Krishna, Z. Di, D. Yuan and M. Wu, *ACS Mater. Lett.*, 2024, **6**, 1388–1395.
42 D. Wang, Z. Shi, W. Li, G. Li, X. Liu and Y. Liu, *Chem. Eng. J.*, 2024, **498**, 155176.
43 T. H. Lee, J. G. Jung, Y. J. Kim, J. S. Roh, H. W. Yoon, B. S. Ghanem, H. W. Kim, Y. H. Cho, I. Pinnau and H. B. Park, *Angew. Chem., Int. Ed.*, 2021, **60**, 13081–13088.
44 A. A. Lysova, K. A. Kovalenko, A. S. Nizovtsev, D. N. Dybtsev and V. P. Fedin, *Chem. Eng. J.*, 2023, **453**, 139642.
45 R. Krishna, *ACS Omega*, 2020, **5**, 16987–17004.
46 G.-D. Wang, R. Krishna, Y.-Z. Li, Y.-Y. Ma, L. Hou, Y.-Y. Wang and Z. Zhu, *ACS Mater. Lett.*, 2023, **5**, 1091–1099.
47 Y.-Z. Li, G.-D. Wang, R. Krishna, Q. Yin, D. Zhao, J. Qi, Y. Sui and L. Hou, *Chem. Eng. J.*, 2023, **466**, 143056.